Understanding multi-layered transmission matrices

Anat Levin and Marina Alterman
Department of Electrical and Computer Engineering, Technion
Haifa, Israel

Abstract

Wavefront shaping systems attempt to correct aberrations caused by tissue scattering, by placing a spatial light modulator (SLM) in the optical path and using it to reshape the light wave emitted from a target of interest deep inside the tissue. However, the field-of-view we can correct with one SLM pattern is extremely small, because inherently the aberration is caused by the 3D tissue structure while the SLM is planar. To overcome this, multi-conjugate correction systems built with multiple layered SLMs have been introduced, which attempt to approximate the 3D tissue structure with multiple planar aberrations.

However, multi-conjugate systems with a large number of SLMs are not easy to construct. Therefore, it is important to understand how many SLM layers are actually needed for a good correction, and whether there are practical benefits from correction systems with a relatively small number of layers. To help in the design of future systems, this paper analyzes multi-layer corrections. We show that the well-known missing cone problem which fundamentally limits the axial resolution of microscopes, turns into an advantage when designing 3D correction systems. Due to this property less information should be captured by the correction system, facilitating sparser approximations. We also show that even if the number of available layers is insufficient for a reasonable approximation of the full 3D tissue volume, it can significantly expand the field-of-view when compared to single-layer correction systems, and therefore can largely accelerate their operation.

1. Introduction

Scattering is a central challenge in multiple imaging tasks ranging from astronomy to microscopy, and biomedical imaging. It degrades our ability to resolve stars through telescopes, image into the bottom of the sea, and drive through foggy weather. Most importantly in the context of this paper, scattering severely limits our ability to image through biological tissue. This happens due to small variations in the refractive index of the tissue volume, which scatters the propagating light.

Numerous computational optics approaches have been developed for imaging through scattering tissue. These include computational restoration algorithms which attempt to fit the observed data with various models for the aberration and the target of interest [4, 5, 15, 17, 21, 23, 25, 32, 37, 39, 40]. Also, optical systems such as a confocal microscope [14] or an OCT [24], aim to filter out the scattered light and maintain only the ballistic unscattered part. However, as we attempt to see deeper into a scattering layer, ballistic light weakens significantly, and the complexity of aberration models increases. Moreover, biological target of interest such as fluorescent tissue components are very weak and as a result the scattered signal is also of a very low signal to noise ratio (SNR), further limiting digital correction models. A particularly attractive approach for scattering aberration removal is wavefront shaping, where one places a spatial light modulator (SLM) in the optical path of the microscope and uses it to correct the wavefront emitted from a point deep inside the tissue, so that light photons emerging from a single target point are brought into a single sensor point, despite the tissue aberration. Wavefront shaping is a particularly attractive solution for fluorescent imaging because the correction is done optically rather than digitally. Unlike ballistic filtering approaches, all light photons are used. Since the correction is done in the optical path, the limited number of available photons is brought into a single detector pixel and can be measured with higher SNR. As a result, wavefront shaping has the potential to revolutionize tissue imaging and allow us to overcome the fundamental limitations of scattering, and image very deep inside biological targets at a high SNR.

The main limitation for wavefront shaping approaches is that the aberrations of neighboring points inside volumetric tissue vary rapidly, and in practice a single correction mask can only allow imaging of a small local field-of-view. This is because the scattering process happens throughout the 3D volume, while the aberration correction only happens on a planar SLM. Earlier demonstrations of wavefront shaping have considered targets placed at a distance behind a thin scattering layer, and this far-field arrangement has allowed them to correct larger regions with a single planar modulation [12, 15, 34, 39]. Similarly in the context of adaptive-optics, researchers have attempted to correct aber-

rations due to imperfect optics or a refractive index mismatch [8, 18, 22]. These aberrations are introduced along the optical path, before the tissue, so the correction can apply to a larger area. However, in most biomedical applications the fluorescent target of interest is embedded within the scattering volume. If our goal is to correct scattering within the tissue itself, the field-of-view which can be corrected by a single planar modulation is extremely small, usually only a few microns [3].

To correct larger fields of view, *multi conjugate* correction systems have been proposed. Such systems use multiple planar SLMs placed such that each of them is conjugate to a different plane inside the tissue volume. Each such SLM should realize a correction for the aberration happening inside a thin layer of the volume and the combination of such multi-plane corrections should approximate the 3D variation in refractive index, and allow us to correct it. Fig. 1 visualizes the concept of a multi-conjugate correction [16, 27, 35, 36]. In practice, multi-plane correction systems are more complicated than the simplified visualization of Fig. 1, as one needs to add multiple relay systems between the SLMs. This is first because there are physical limitation on the minimal distance between 2 SLMs, and second because we need to revert the order of the correction layers in the inversion path [19]. This makes multi-conjugate correction systems complex and cumbersome to build. Previous experimental demonstrations have realized corrections with no more than two SLMs. While two-layer correction systems have demonstrated improved performance compared to single layer correction, two planes clearly cannot model a thick 3D tissue structure.

Our goal in this research is to analytically study multi-slice models and attempt to answer the following questions: How many planes are required to approximate the 3D aberration of a scattering tissue volume? How does the quality of the correction degrade if we use a sparser approximation? If a construction of a practical correction system is limited to only to M layers, what is the maximum field of view that can be effectively corrected?

To this end, we use the mathematical model of a transmission matrix, which stores the propagation of coherent wavefronts from one end of a scattering volume to the other. We study how well we can approximate such transmission matrices with a multi-slice model, and how does the error depend on the number of fitted layers.

The straightforward answer to this question is to say that the spacing between layers should match the axial resolution of the microscope. For example, using an **NA** $= 0.5$ objective at wavelength $500nm$, we get that the spacing between layers should be lower than $2\mu m$. Handling a modest tissue thickness of, e.g., $200\mu m$ already requires 100 slices for a valid approximation. Clearly building a multi-conjugate wavefront shaping systems with so many layers
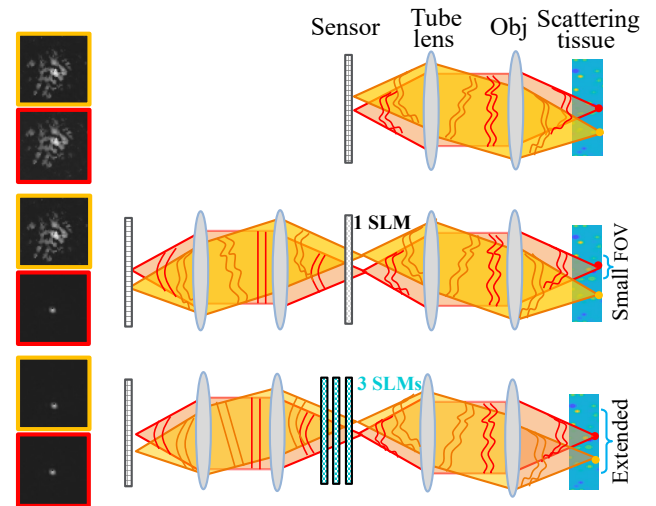

Figure 1. **Layered wavefront shaping:** (Top) Consider a simple microscope setup where we use a 4F relay to image the light emerging from a tissue sample. Light is aberrated on its way to the sensor, and we see speckle patterns rather than sharp spots. (Middle) A single planar SLM can correct aberration for one spot (see red beam), but light emerging from nearby spots may not be corrected (the yellow beam generates a speckle pattern on the sensor). (Bottom) The field of view of the correction can possibly be extended with a multi-layer correction. The goal is to form a correction replicating the 3D structure of volumetric aberration inside the tissue. The figure illustrates two wavefronts from nearby spots (red and yellow) passing through the same volumetric correction, and both focus into a sharp spot behind the tissue.

is impractical.

In this research we take inspiration from [20], and offer a thorough analysis of the frequency content of transmission matrices, combining the forward scattering nature of biological tissue with the structure of the missing cone. We show that while the missing cone structure is known as one of the fundamental limitations of 3D microscopy, in the context of transmission matrices this limitation turns into an advantage. Due to the missing cone structure, many of the frequencies of the volumetric aberration do not participate in the transmission matrix, and therefore the number of layers required for approximating a transmission matrix is way smaller than the Nyquist limit. However, there are no free lunches and the number of layers scales with the tissue thickness. To explain a few hundred micron thick tissue one needs a few dozen layers, which is still too much to be realized by a physical correction system.

Given this conclusion we aim to understand if there are any practical benefits in realizing a multi-conjugate correction system with a small number of say $2-4$ layers. We show that while a small number of layers cannot well approximate the 3D structure of the tissue, it can allow us to realize a correction over a limited field-of-view. The area which can be corrected with M aberration layers is significantly larger than the area which can be corrected with one layer, and therefore it can significantly accelerate sequen-

(a) Full setup   (b) Fourier illum.   (c) Point illum.   (d) Layered approx.
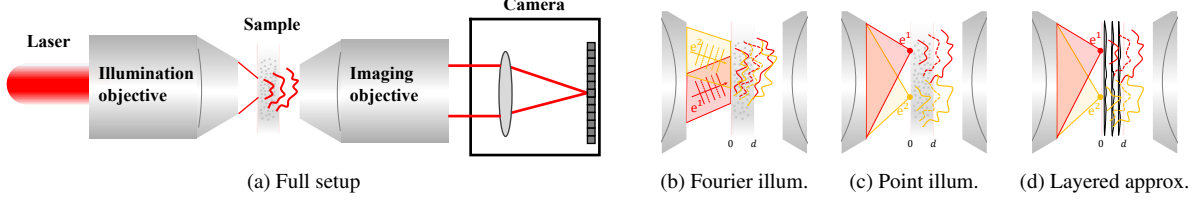
Figure 2. **Setup for transmission matrix acquisition:** (a) A setup for transmission matrix imaging where a set of basis illuminations at the back of the sample propagate through the volume, and the scattered wavefronts are measured by a camera at the other end. In (b,c) we zoom on the sample illustrating two possible illumination bases. (b) A set of directional wavefronts (Fourier basis). (c) A set of wavefronts focused to points at the edge of the volume (primal basis). Both transmission matrices can be related by a simple Fourier transform. (d) A multi-slice model approximates the volumetric scattering with a set of planar aberrations.

tial correction of the field of view. We validate our findings using real transmission matrices captured in the lab as well as synthetic transmission matrices simulated using accurate wave propagation models.

2. Problem formulation

Imaging setup: For simplicity, the following derivation considers coherent scalar waves, ignoring polarization. In Fig. 2(a) we visualize a setup for transmission matrix acquisition. A scattering medium, such as tissue, is illuminated by a coherent source $\mathbf{e}^k$ at one side of the medium. After propagating through the medium, the resulting coherent wavefront $\mathbf{t}^k$ is recorded. Usually $\mathbf{t}^k$ are complex valued speckle patterns with a pseudo-random structure. The illumination is translated and multiple wavefronts are recorded and stored as columns of a transmission matrix $\mathcal{T}$.

The transmission matrix: Since the propagation of coherent light is linear, if we want to predict the propagation of any wavefront $\mathbf{u}$, we simply express it as a superposition of the recorded incoming illuminations $\mathbf{u} = \sum_k \mathbf{u}(k)\mathbf{e}^k$, where $\mathbf{u}(k)$ are complex scalars, and multiply it by the transmission matrix, to predict $\mathcal{T}\mathbf{u}$. The illumination wavefronts $\mathbf{e}^k$ can be selected at different bases. For example, the illumination can be translated at the Fourier plane, and then the wavefronts illuminating the sample are plane waves at different angles (Fig. 2(b)). Alternatively one can focus the light to a point at the back plane of the sample (Fig. 2(c)). This configuration is more appropriate for wavefront shaping algorithms whose goal is to recover wavefronts focusing inside the tissue and not far behind it. In both cases, however, the illuminations we can create are limited by the numerical aperture of the illuminating objective, which we mark here as $\mathbf{NA}$. Similarly, the scattered wavefronts are measured via an imaging objective with the same bounded $\mathbf{NA}$. This $\mathbf{NA}$ would serve as a central component in the results derived below. For simplicity of resulting equations, for the rest of this manuscript we assume the imaging and illumination objectives are focused at the same plane, such that if we would remove the scattering sample and image the sources directly, we would see the $\mathbf{e}^k$ illuminations as sharp spots on the sensor plane. That is, if we use directional

illuminations, we also measure the Fourier transform of the scattered waves, namely place the sensor at the Fourier plane of the imaging objective. If we use point sources at the illumination end of the medium, we also focus the imaging objective at the same plane, so we measure a speckle image of a relatively small support.

Range and resolution: We assume that in the primal basis the illuminators are spaced within an area of $\mathbf{\Omega_p} \times \mathbf{\Omega_p}$, and we sample them at the Nyquist resolution, so for an illumination wavelength λ they are separated by a pitch $\mathbf{\Delta_p} = \lambda/(2\mathbf{NA})$. Equivalently, in the Fourier domain, we illuminate the sample with plane waves of the form

$$\mathbf{e}(\mathbf{r}) = e^{2\pi i(\bar{\boldsymbol{\kappa}} \cdot \mathbf{r})} \tag{1}$$

where $\mathbf{r}$ is a point inside the 3D volume, and $\bar{\boldsymbol{\kappa}} = \frac{1}{\lambda}\bar{\boldsymbol{\omega}}$ where λ is the wavelength and $\bar{\boldsymbol{\omega}}$ is a unit norm direction vector, i.e. the last entry of the direction vector ω_z is $\omega_z = \sqrt{1-(\omega_x^2 + \omega_y^2)}$. For simplicity of notation, we assume the refractive index (RI) of the leading medium is 1. We can only use illumination direction inside the numerical aperture $\sqrt{\omega_x^2 + \omega_y^2} \leq \mathbf{NA}$ (or equivalently $\sqrt{\kappa_x^2 + \kappa_y^2} \leq \mathbf{\Omega_f}$ with $\mathbf{\Omega_f} = \mathbf{NA}/\lambda$). To sample the transmission matrix at the Nyquist pitch, the κ_x, κ_y components of the illumination are sampled by the Nyquist pitch $\mathbf{\Delta_f} = 1/2\mathbf{\Omega_p}$.

With the above sampling scheme, the transmission matrices at the Fourier and primal bases are related by a simple Fourier transform $\mathcal{T}^p = \mathcal{F}^T \mathcal{T}^f \mathcal{F}$. While for wavefront shaping we are interested in primal transmission matrices, the Fourier ones simplify analysis. Importantly, since Fourier and primal transmission matrices are related by an orthonormal transformation, the fitting errors in both bases are equivalent.

The multi-slice model: The relation between an incoming illumination and an outgoing one is determined by the solution to a wave equation which takes into account the variation in refractive index (RI) inside the sample. Rather than a fully continuous model, in a multi-slice model we approximate the volume with a set of planar aberrations, separated by small z distances Δ_z, where we have free space propagation between layers, as in Fig. 2(d). Mathematically this can be described as

$$\mathcal{T}(\boldsymbol{\rho}_1, \ldots, \boldsymbol{\rho}_M) = \mathcal{P}_O \mathcal{D}(\boldsymbol{\rho}_M) \ldots \mathcal{P}_{\Delta_z} \mathcal{D}(\boldsymbol{\rho}_2) \mathcal{P}_{\Delta_z} \mathcal{D}(\boldsymbol{\rho}_1), \tag{2}$$
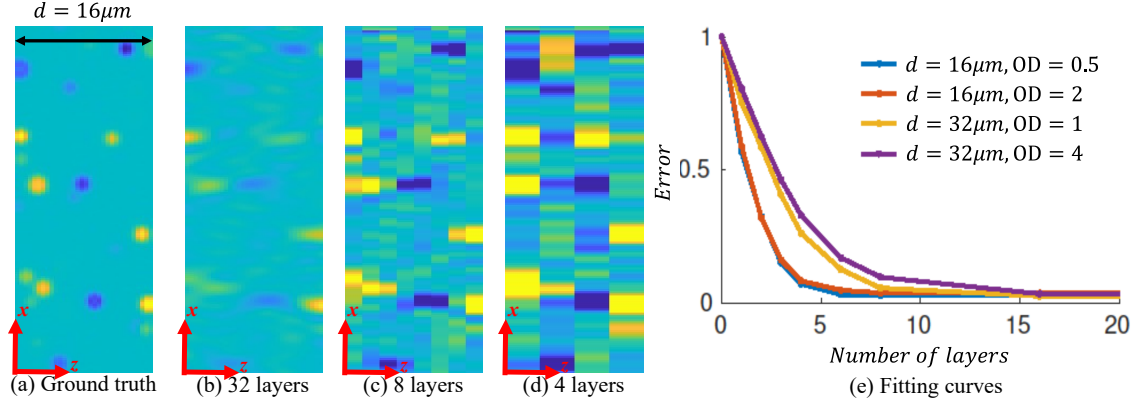
Figure 3. Reconstructed volumes: (a) An xz slice from a toy volume, visualizing its refractive index variations. (b-d) Reconstructions with varying layer numbers. The columns of the transmission matrix provide an under-constraint inversion problem, and even when a dense set of layers is allocated in b, the axial resolution of the reconstructed volume is low. As a result the sparse reconstructions in c,d can also well explain the transmission matrix. (e) Numerical evaluation of fitting error as a function of the number of layers. Transmission matrices can be well fitted even if the allocated number of layers is lower than Nyquist predictions. However the required number of layers increases with the tissue thickness. The layer number is less affected when the optical density is increased for the same tissue thickness.

where $\boldsymbol{\rho}_m(x,y)$ is the 2D aberration of the mth layer and $\mathcal{D}(\boldsymbol{\rho}_m)$ is a diagonal matrix performing element-wise multiplication of the incoming wavefront by the aberration. $\mathcal{P}_{\Delta_z}$ describes free space propagation between layers at distance Δ_z, which is essentially a convolution with a spherical wavefront. Finally $\mathcal{P}_O$ propagates the wavefront in free space from the tissue boundary, via the lenses, to the camera sensor.

Our goal is to understand what plane spacing Δ_z will facilitate a good representation of $\mathcal{T}$, and how this approximation would degrade when we use sparser sampling.

A common approximation for weak aberrations is:

$$\boldsymbol{\rho}_m(x,y) = \mu + \boldsymbol{\delta\rho}_m(x,y), \qquad (3)$$

where μ is a scalar whose magnitude is a bit smaller than 1, encoding the ballistic portion of the light which passes through the layer without aberration, and the magnitude of the aberration is significantly smaller than the ballistic term $|\boldsymbol{\delta\rho}_m(x,y)| \ll |\mu|$. For weak scattering most of the energy does not scatter more than once. It is therefore common to consider a first order approximation to the transmission matrix (often known as the single scattering, first-Born or Rytov approximation [9, 10, 13, 29, 33]), which reduces to

$$\mathcal{T}(\boldsymbol{\delta\rho}_1,\ldots,\boldsymbol{\delta\rho}_M) \approx \mu^M \mathcal{P}_O \mathcal{P}_{M\Delta_z} + \qquad (4)$$

$$\mu^{M-1}\sum_{m=1}^{M}\mathcal{P}_O\mathcal{P}_{(M-m)\Delta_z}\mathcal{D}(\boldsymbol{\delta\rho}_m)\mathcal{P}_{m\Delta_z}$$

The full light propagation in Eq. (2) includes multiplication of the different aberrations and hence the transmission matrix is highly nonlinear. In contrast, the advantage of the weakly scattering model in Eq. (4) is that the resulting transmission matrix is a linear function of the aberration layers. This linear approximation significantly simplifies analysis.

Diffraction tomography algorithms such as [11] capture a subset of columns from the transmission matrix and use gradient descent optimization to seek layers $\boldsymbol{\rho}_1,\ldots,\boldsymbol{\rho}_M$ which best explain the measured wavefronts, assuming that the propagation operators $\mathcal{P}_{\Delta_z}, \mathcal{P}_O$ are known. We will use a similar optimization scheme below, when trying to find a multi-slice representation for a given transmission matrix. To correct aberrations, a physical multi-conjugate wavefront shaping system would display on the SLM the conjugate of the recovered layers.

3. Evaluating multi-slice approximations

We start with numerical experiments demonstrating the main findings. In Sec. 4 below we derive a theory explaining them. To gain intuition we generated a toy volume composed of spheres with varying refractive indices illustrated in Fig. 3(a), and obtained the corresponding transmission matrix by propagating a set of point sources through the volume. We then used the transmission matrix to solve for a multi-slice approximation, while varying the number of layers. In Fig. 3(b-d) we visualize some of the volumetric reconstructions, assuming a $\lambda = 500nm$ illumination. Even when the fitted layers are sampled very densely at an interval of $\Delta_z = 0.5\mu m$, we cannot fully recover the target and the fitted volume has a low axial resolution. We analyze this in Sec. 4 below and explain that this results from the well known missing cone problem, a fundamental degeneracy limiting the axial resolution of a microscope. Said differently the transmission matrix, or the full set of propagating waves, only provides a set of under-constraint measurements from which the volume cannot be uniquely recovered. While the missing cone problem is considered a fundamental limitation in microscopy, we argue that in the context of wavefront shaping it actually turns into an advantage. Since the volume reconstruction is not unique we can
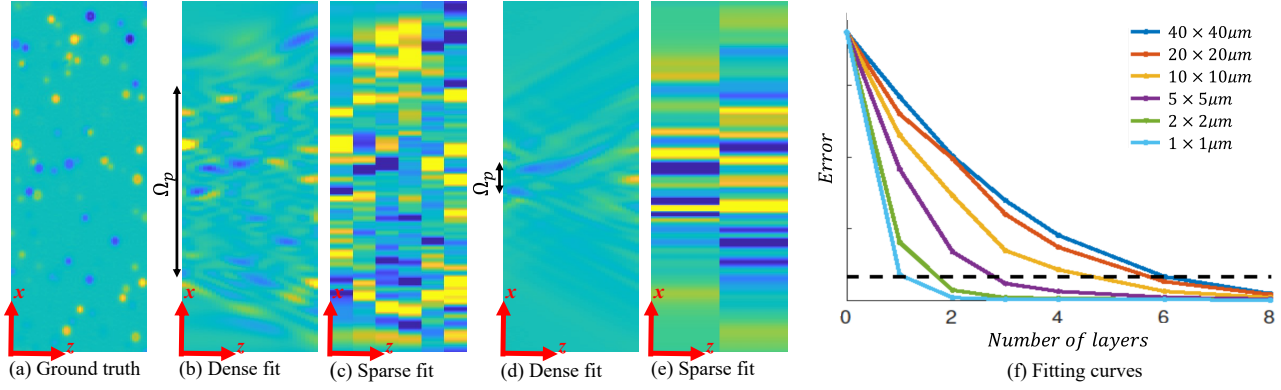
Figure 4. **Reconstructed volumes with varying supports:** (a) An xz slice from a toy volume, visualizing its refractive index variations. (b,d) Two reconstructions of the volume using a dense layer sampling. When the support of the measured window $\boldsymbol{\Omega_p}$ shrinks, the lateral extent of the reconstructed region decreases, however, its axial resolution is also reduced. (c,e) A sparse fit with the same input. Despite the low quality of these reconstructions, they predict well the columns of the transmission matrix of the given support $\boldsymbol{\Omega_p}$. (f) Numerical evaluation of fitting error as a function of the number of layers, while varying the range $\boldsymbol{\Omega_p}$ covered by the transmission matrix. Smaller supports can be fitted with fewer layers.

approximate the same transmission matrix with a sparser set of layers.

To quantify the fitting error of the multi-slice model, we denote by $\mathcal{E}_M$ the reconstruction error of a given transmission matrix with the best M layers

$$\mathcal{E}_M = \min_{\boldsymbol{\rho}_1,\ldots,\boldsymbol{\rho}_M} \|\mathcal{T}_{\text{exact}} - \mathcal{T}(\boldsymbol{\rho}_1,\ldots,\boldsymbol{\rho}_M)\|^2. \qquad (5)$$

In Fig. 3(e) we evaluate $\mathcal{E}_M$ as a function of the layer number M. Even the seemingly aliased fit of Fig. 3(d) still provides a low fitting error. However, there are no free lunches and when the number of layers is too low the fitting error is high. When we repeat the simulation with a thicker volume we need even more layers for a good fit. Interestingly, we also repeat the simulation with denser volumes (larger optical depth, or shorter mean free path) of the same thickness, and this has less effect on the required number of layers. In our plots, the case $M = 0$ refers to no correction at all, so effectively we assume that the transmission matrix is diagonal. The similarity between a diagonal transmission matrix and the target transmission matrix is a measure of the amount of ballistic light.

The thickness of the synthetic simulation here is limited due to computational constraints. However, usually wavefront shaping systems attempt to see into a few hundred microns of tissue and we anticipate that for such volumes we need at least a few dozen layers for a good fit. Clearly realizing a physical wavefront shaping system with that many layers is impractical. We argue that while a small number of layers is not enough for focusing light anywhere across the tissue area, it can still help us to focus light over a compact support area, and this area is significantly wider than what we can correct with a single layer.

Compact support: To test the effect of the target area, we consider transmission matrices measured with illumination points confined to a limited area of size $\boldsymbol{\Omega_p} \times \boldsymbol{\Omega_p}$. If we can

fit such a transmission matrix with M layers and place the values of these M layers on M SLMs, the resulting wavefront shaping system can correct light from the $\boldsymbol{\Omega_p} \times \boldsymbol{\Omega_p}$ area, but target points outside this area are unlikely to be corrected as they are not included in the fitting process.

To test the effect of support on the number of fitted layers, we return to the numerical simulation of Fig. 3, but fit subsets of columns contained in smaller $\boldsymbol{\Omega_p}$ ranges. Indeed, smaller supports can be well-fitted with a smaller number of layers. As another way to understand it, we show in Fig. 4 an xz slice from the ground truth refractive index volume and from a few reconstructions. We show that even if we do not limit the layer number M, the recovered RI volume has limited axial resolution and this axial resolution is lower when measured range $\boldsymbol{\Omega_p}$ decrease. This explains why lower supports can be fitted with fewer layers. For each of the two supports we also show a sparse fit, with the minimal M value that provides a good prediction of the transmission matrix. We explain this observation in Sec. 4. This result is also in agreement with [26], who correct aberration over a relatively *small field of view* through a few hundred microns of tissue, using only 5 layers.

Implications to layered wavefront shaping systems. In Fig. 4(f) we plotted a bar below which the approximation is reasonable. We can see that for e.g. the $40 \times 40\mu m$ support we can obtain good focusing with about $M = 6$ layers. It is likely that fitting a full field-of-view of a few hundred microns would require more layers. However, we can see that while with $M = 1$ layer we could only focus over a small area of about $1 \times 1\mu m$, when increasing to $M = 2$ we could focus over a $\times 4$ larger area of support $2 \times 2\mu m$, and with $M = 3$ we could focus over a $\times 25$ larger area of support $5 \times 5\mu m$. Computing multiple correction elements is only going to increase the complexity of the wavefront shaping
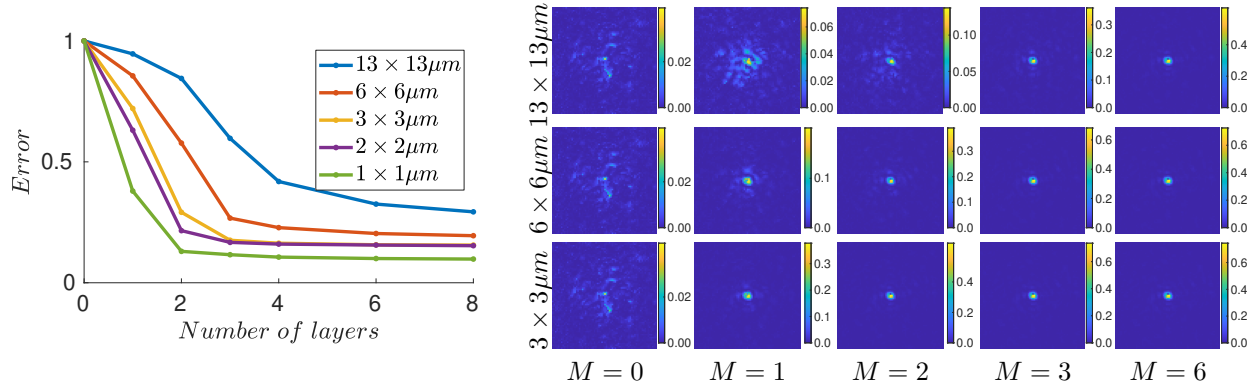
Figure 5. **Layer support for a captured transmission matrix:** We consider a transmission matrix captured in the lab through a chicken breast layer of thickness $170\mu m$. Left: plotting the fitting error as a function of the number of layers. Smaller supports can be fitted with fewer layers. Right: Visualization of a spot focusing behind the tissue computed using the wavefronts of the fitted model. We compare models fitted to different supports. In the top row we need a larger number of layers, but the spot can be scanned over a $25 \times 25\mu m$ window using the same layers. In the lower rows we achieve a focused spot using a smaller number of layers, but these layers can scan the focused spot over smaller windows of sizes $6 \times 6\mu m$ and $1 \times 1\mu m$.

algorithm in [1] linearly with the number of layers. Alternatively, a wavefront shaping system using a single SLM would need to scan the field-of-view sequentially and correct each local window independently. Since the increase in the support of the window we can explain with e.g. 3 layers is significantly larger than a $\times 3$ factor, a multi-conjugate wavefront shaping system with a small number of SLMs as in [16, 27, 31, 35] can already have a large practical benefit. While Fig. 4 only considers a simulation, we analyze realistic numbers below.

Lab results: In the supplementary file we validate the theory with multiple real transmission matrices, representing thick volumes with multiple-scattering.

We start with numerically simulated transmission matrices using a more accurate wave-propagation model [6, 7]. We then test lab-captured transmission matrices measuring realistic scattering samples including mouse brain tissue, chicken breast tissue and a parafilm layer. *Please refer to supplementary file for additional results*.

In Fig. 5 we show one fitting result using a multiply-scattering chicken breast layer of thickness $d = 170\mu m$. The transmission matrices cover an area with support $\Omega_p \times \Omega_p = 13 \times 13\mu m$. As in Fig. 4(f), we see that smaller spatial ranges can be fitted with fewer layers.

As another way to asses the quality of the fit, we used columns of the fitted matrices to focus light through the tissue and show the shape of the focused spot and visualize the focusing quality in Fig. 5. To simulate the focused spot we simply visualize the product $\mathcal{T}_{\text{exact}} \cdot \mathbf{t}_{\text{fit,M}}^k$, where $\mathbf{t}_{\text{fit,M}}^k$ is a column of the fitted matrix $\mathcal{T}(\boldsymbol{\rho}_1, \ldots, \boldsymbol{\rho}_M)$, namely a wavefront generated by the layered approximation. Note that while we only show focusing at one point, the layers are optimized such that they allow us to focus at *any point* inside the $\Omega_p \times \Omega_p$ window.

From the results in Fig. 5 we can see that for the $13 \times$

$13\mu m$ support measured, we can obtain good focusing with about 3 layers. Fitting a full field-of-view of several hundred microns likely requires additional layers. However, we observe that while using $M = 1$ allows us to focus on a small area of about $3 \times 3\mu m$, with $M = 3$, we can focus on an area $\times 18$ larger, reaching $13 \times 13\mu m$. Therefore, using multiple layers can significantly accelerates a sequential scanning of a wave-front shaping system.

4. Sampling theory for transmission matrices

Our goal in this section is to explain the empirical findings of the previous section by analyzing the information captured by a transmission matrix.

4.1. Nyquist sampling and the missing cone

We start by considering the case of weakly scattering volumes which, as in Eq. (4), can be reasonably approximated by considering the component of light that scattered once. We also assume the transmission matrix is sampled over a very wide support Ω_p. We discuss the implications of multiple scattering and limited supports in subsequent sections.

We denote by $\boldsymbol{n}(\mathbf{r})$ the difference between the RI at a 3D position $\mathbf{r}$ in the volume to that of the leading medium around it. We denote its 3D Fourier transform by $\hat{\boldsymbol{n}}(\boldsymbol{\kappa})$.

We start by considering the Fourier representation of the transmission matrix, where it is illuminated and measured by plane waves. Using the weakly scattering (first-Born) approximation, the wavefront scattering toward direction $\bar{\boldsymbol{\omega}}^v$ when illuminated by an incoming plane wave at direction $\bar{\boldsymbol{\omega}}^i$ is proportional, up to a multiplicative factor, to [28, 30, 38]:

$$\propto \int \boldsymbol{n}(\mathbf{r}) e^{2\pi i (\bar{\boldsymbol{\kappa}}^i - \bar{\boldsymbol{\kappa}}^v) \cdot \mathbf{r}} d\mathbf{r}, \qquad (6)$$

with $\bar{\boldsymbol{\kappa}}^v = 1/\lambda \bar{\boldsymbol{\omega}}^v$, $\bar{\boldsymbol{\kappa}}^i = 1/\lambda \bar{\boldsymbol{\omega}}^i$. This implies that effectively an entry of the transmission matrix is a sample
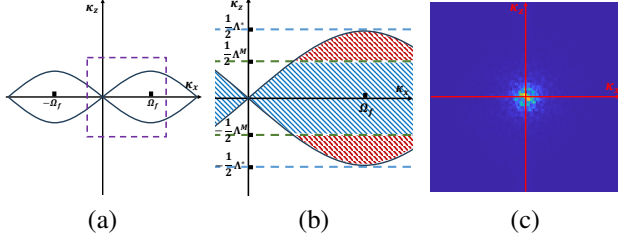
(a)   (b)   (c)

Figure 6. **Spectrum structure:** (a) An xz slice out of the spectrum of $\hat{\boldsymbol{n}}(\boldsymbol{\omega})$. Entries of a weakly-scattering transmission matrix limited by an aperture **NA** only lie inside the butterfly area. (b) Zooming on the center right area of (a) (purple square). Assuming the ω_z axis is cut at $\pm\frac{1}{2}\Lambda^M$, the transmission matrix entries inside the dashed blue area are maintained, and the entries in the dashed red area are lost. (c) The energy at a slice from the spectrum of the volume in Fig. 3(a). Since the volume structure is smooth, most energy is concentrated at the low frequencies. As a result the cropped red region in (b) do not contain a lot of energy.

from the 3D Fourier transform of the volume at frequency $\boldsymbol{\kappa} = \bar{\boldsymbol{\kappa}}^i - \bar{\boldsymbol{\kappa}}^v$. Note that throughout this paper we use bars $\bar{\boldsymbol{\omega}}, \bar{\boldsymbol{\kappa}}$ to denote vectors with norm constraints, and use normal bold fonts to denote standard 3D vectors, such as frequencies $\boldsymbol{\kappa}$ in the 3D spectrum. Unfortunately, a large portion of the 3D spectrum cannot be measured. Recalling that the illumination and viewing directions are limited by an aperture of width **NA**, the subset of 3D frequencies captured by the transmission matrix occupies only a butterfly shape, and the rest of the cone is missing, see illustration in Fig. 6(a). Using paraxial approximation it can be shown [28, 38] that the range of frequencies which can be generated is

$$|\kappa_z| \leq \mathbf{NA}|\boldsymbol{\kappa}_{xy}| - \frac{\lambda}{2}|\boldsymbol{\kappa}_{xy}|^2, \quad \text{with} \quad |\boldsymbol{\kappa}_{xy}| = \sqrt{\kappa_x{}^2 + \kappa_y{}^2}. \tag{7}$$

The missing cone is a serious problem for diffraction tomography algorithms aiming to recover the 3D structure of the refractive index $\boldsymbol{n}(\mathbf{r})$ from columns of the transmission matrix, since many of the frequencies of the volume cannot be recovered. We argue that in the context of transmission matrices, the missing cone problem turns into an advantage. The fact that the transmission matrix only captures a limited range of frequencies allows us to approximate it with fewer samples, as derived below.

Minimal sampling: Our goal is to approximate a transmission matrix with layers. We start by asking what spacing between layers will allow an exact reconstruction of the transmission matrix. If we approximate the volume $\boldsymbol{n}(\mathbf{r})$ with a set of planes, we essentially sample a continuous signal. Classical Nyquist theory states that if we sample a signal at intervals of Δ_z, its Fourier transform includes replicas spaced by $\Lambda = 1/\Delta_z$. To achieve a good reconstruction, we want replicas to happen only in areas of the spectrum that the transmission matrix does not sample. Since the κ_x, κ_y components of our illuminations are limited by the aperture $|\boldsymbol{\kappa}_{xy}| \leq \boldsymbol{\Omega}_f$, and given the butterfly shape in Eq. (7), the κ_z

frequencies we need to maintain are bounded to

$$|\kappa_z| \leq \frac{\mathbf{NA}\boldsymbol{\Omega}_f}{2}. \tag{8}$$

Therefore, for an error-free reconstruction, the minimal Fourier range and primal spacing are

$$\Lambda^* = \mathbf{NA}\boldsymbol{\Omega}_f, \quad \Delta_z{}^* = \frac{1}{\mathbf{NA}\boldsymbol{\Omega}_f} = \frac{\lambda}{\mathbf{NA}^2}. \tag{9}$$

For a scattering volume of thickness d, the number of required layers is:

$$M^* = \frac{d \cdot \mathbf{NA}^2}{\lambda}. \tag{10}$$

For typical numbers, consider e.g. $\lambda = 0.5\mu m$ and $\mathbf{NA} = 0.5$, the plane spacing should be relatively small, and $\Delta_z \leq 2\mu m$. For a modest tissue thickness of $d = 200\mu m$, we will need $M = 100$ planes. Clearly it is impractical to realize such a large number of planes by a physical correction system.

4.2. Sparse multi-slice approximations

Consider a scattering sample of thickness d, which we try to approximate using $M < M^*$ layers separated by $\Delta_z = \frac{d}{M}$. Our goal is to show that the fitting error $\mathcal{E}_M$ defined in Eq. (5) decays relatively fast with M and we can get a reasonable approximation to the transmission matrix even if the number of layers is lower than the exact prediction in Eq. (10). This is a result of two main properties: (i) The volumes describing realistic tissue samples have more energy in the low frequencies; and (ii) the structure of the missing cone implies that, in any case, a significant portion of the spectrum is not sampled by the transmission matrix.

To understand this, consider a naive selection of M layers $\boldsymbol{\rho}_1, \ldots, \boldsymbol{\rho}_M$. Rather than actually solving an optimization problem, we use the ground truth volume $\hat{\boldsymbol{n}}(\boldsymbol{\kappa})$, and simply set to zero any frequency content of the RI volume $\hat{\boldsymbol{n}}(\boldsymbol{\kappa})$ at κ_z values larger than the possible Nyquist range

$$\Lambda^M = \frac{1}{\Delta_z} = \frac{\lambda M}{d}, \tag{11}$$

and we then Fourier transform $\hat{\boldsymbol{n}}(\boldsymbol{\kappa})$ to $\boldsymbol{n}(\mathbf{r})$ and sample planes at spacing $\Delta_z = d/M$. The error of this approximation is basically the integral of content above the cut-off Λ^M. Since according to Eq. (11), the cut-off frequency Λ^M scales linearly with the number of layers, the portion of the spectrum which is lost by this low-pass operation scales linearly with the number of layers M. Thus, the naive answer is that the error of a multi-slice approximation decays linearly with M. In practice we show below that the error decays much faster, since *large areas from the 3D spectrum of the sample are not used by the transmission matrix.*

To gain intuition, consider Fig. 6(b). We note that the butterfly shape is such that low 2D frequencies (i.e. low $|\boldsymbol{\kappa}_{xy}|$), also span less content along the κ_z axes, and hence these frequencies are not lost even with low bandwidths Λ^M. For the higher $|\boldsymbol{\kappa}_{xy}|$ frequencies, the lower κ_z part, marked in dashed blue in Fig. 6(b) is preserved, while the higher portion marked in red is lost.

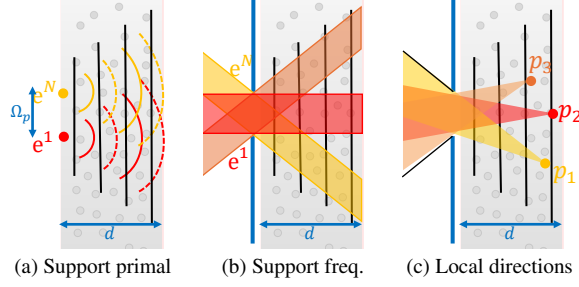(a) Support primal   (b) Support freq.   (c) Local directions

Figure 7. **Layer support:** (a) As point sources expand while propagating through the volume, the width of the aberration layers should be wider than the measured support $\mathbf{\Omega_p}$. (b) To express compact support transmission matrices in the Fourier basis, we illuminate the volume by a set of plane waves passing through an aperture. (c) The local cone of illumination angles reaching different points inside the volume is much smaller than the actual range of incoming illuminations.

Another important property of tissue is that its RI is locally smooth, and therefore if we look at its spectrum (Fig. 6(c)), we have much more energy in low frequencies than in high ones. This also agrees with the fact that tissue is forward scattering. Therefore, in the red areas of Fig. 6(b) that are not sampled by the transmission matrix, there is less energy than in the lower frequencies. Thus, despite the fact that the multi-slice approximation sacrifices such frequencies, not much energy is being lost.

In most cases, it is hard to give analytic formulas for the decay of $\mathcal{E}_M$ as a function of M, but the supplementary file contains some derivation under simplifying assumptions.

Multiple scattering. The results in Fig. 3(e) include multi-slice fits with both lower and higher optical depth values up to $OD = 4$, showing that the fitting error still decays rapidly with the number of layers.

While it is hard to give analytical predictions for the multiple scattering case, it appears that when the optical depth of the tissue is not too high, similar results hold. The reason is that for a forward-scattering material such as tissue, light paths only scatter at small angles, and after a small number of scattering events they are not completely scrambled. For an intuition, in the supplementary file we use a Monte-Carlo simulation illustrating that for a forward-scattering material, after a modest number of scattering events, most light paths still remain within the butterfly area of the spectrum. This is usually the regime that wavefront-shaping algorithms like [1, 2] attempt to tackle, as such algorithms attempt to push the depth at which conventional microscopes can see, but they do not yet attempt to image extremely deep where scattering is fully diffused.

4.3. Bounded support matrices

As stated above, much fewer layers are needed if we only attempt to fit transmission matrices sampled over a small area of size $\mathbf{\Omega_p} \times \mathbf{\Omega_p}$.

When fitting layers, we need to account for the fact that a point/plane illumination scattering through a volume is expanding. Thus, the aberration layers required to explain the transmission matrix are wider than the imaged area of size $\mathbf{\Omega_p} \times \mathbf{\Omega_p}$, see Fig. 7(a). Expressing a transmission matrix with a compact support at the frequency basis is equivalent to illuminating the sample with plane waves spanning a wide set of angles, but all the waves pass through a narrow aperture of size $\mathbf{\Omega_p} \times \mathbf{\Omega_p}$. In this case most points inside the volume usually do not receive light from all angles. In Fig. 7(c) we plot the narrow cone of angles arriving at three different points (a ray leaving a point $\mathbf{p_j}$ at angle $\bar{\omega}$ is included in the cone only if this angle is not cropped by the aperture at the back of the sample). Since the cone of light reaching each point is narrower than the full numerical aperture, a local Fourier transform would not have content over the full butterfly area, but cover an even lower range of axial ω_z frequencies. Hence, following the analysis in the previous section, it can be sampled with fewer layers. We visualize the local spectra in the supplement.

5. Discussion

This paper studies how well we can fit transmission matrices with multi-slice models and how many layers are needed in practice. We show that the required number of layers is much lower than the prediction of Nyquist sampling theory. This is because the missing cone problem of 3D microscopy turns into an advantage when analyzing transmission matrices. Moreover, as tissue is forward scattering, its 3D spectrum contains most energy in the low frequencies and much less energy in the higher ones. Hence, even if the sparse sampling acts as a low-pass on the large axial frequencies, not much energy is lost.

We validate this prediction using both synthetic simulations and realistic lab measurements. We show that even though realistic transmission matrices contain backward and side-ward scattering which are not modeled by multi-slice matrices, they provide a reasonable approximation that is good enough for wavefront shaping focusing.

Our findings suggest that multi-slice models can be applicable for the design of non-local wavefront shaping systems, allowing for a volumetric correction with a small number of layered SLMs [16, 27, 35, 36]. Even if $2 - 3$ SLM layers may not be enough for correcting the full field-of-view of a wide image through a thick tissue, they can allow us to increase the support of the fitted area by much more than $\times 2 - 3$ thus they can significantly accelerate a sequential wavefront-shaping correction of a wide image.

Code and data: can be obtained at https://webee.technion.ac.il/people/anat.levin/papers/LayerdTmat_cvpr25_code.zip

References

[1] Dror Aizik and Anat Levin. Non-invasive and noise-robust light focusing using confocal wavefront shaping. *Nature communications*, 15(5575), 2024.

[2] Dror Aizik, Ioannis Gkioulekas, and Anat Levin. Fluorescent wavefront shaping using incoherent iterative phase conjugation. *Optica*, 9(7):746–754, 2022.

[3] M. Alterman, C. Bar, I. Gkioulekas, and A. Levin. Imaging with local speckle intensity correlations: theory and practice. *ACM TOG*, 2021.

[4] YoonSeok Baek, Hilton B. de Aguiar, and Sylvain Gigan. Phase conjugation with spatially incoherent light in complex media. *Nature Photonics*, 17(12):1114–1119, 2023.

[5] Paul Balondrade, Victor Barolle, Nicolas Guigui, Emeric Auriant, Nathan Rougier, Claude Boccara, Mathias Fink, and Alexandre Aubry. Multi-spectral reflection matrix for ultrafast 3d label-free microscopy. *Nature Photonics*, 18(10):1097–1104, 2024.

[6] Chen Bar, Marina Alterman, Ioannis Gkioulekas, and Anat Levin. A monte carlo framework for rendering speckle statistics in scattering media. *ACM TOG*, 2019.

[7] Chen Bar, Ioannis Gkioulekas, and Anat Levin. Rendering near-field speckle statistics in scattering media. *ACM TOG*, 2020.

[8] Martin Booth. Adaptive optical microscopy: The ongoing quest for a perfect image. *Light: Science and Applications*, 3:e165, 2014.

[9] Bingquan Chen and Jakob J. Stamnes. Validity of diffraction tomography based on the first born and the first rytov approximations. *Appl. Opt.*, 37(14):2996–3006, 1998.

[10] Wonshik Choi, Christopher Fang-Yen, Kamran Badizadegan, Seungeun Oh, Niyom Lue, Ramachandra R Dasari, and Michael S Feld. Tomographic phase microscopy. *Nature methods*, 4(9):717—719, 2007.

[11] Shwetadwip Chowdhury, Michael Chen, Regina Eckert, David Ren, Fan Wu, Nicole Repina, and Laura Waller. High-resolution 3d refractive index microscopy of multiple-scattering samples from intensity images. *Optica*, 6(9):1211–1219, 2019.

[12] Anat Daniel, Dan Oron, and Yaron Silberberg. Light focusing through scattering media via linear fluorescence variance maximization, and its application for fluorescence imaging. *Optics Express*, 27(15):21778, 2019.

[13] A. J. Devaney. Inverse-scattering theory within the rytov approximation. *Opt. Lett.*, 6(8):374–376, 1981.

[14] Amicia D. Elliott. Confocal microscopy: Principles and modern practices. *Current Protocols in Cytometry*, 92(1):e68, 2020.

[15] Brandon Y. Feng, Haiyun Guo, Mingyang Xie, Vivek Boominathan, Manoj K. Sharma, Ashok Veeraraghavan, and Christopher A. Metzler. Neuws: Neural wavefront shaping for guidestar-free imaging through static and dynamic scattering media. *Science Advances*, 9(26):eadg4671, 2023.

[16] T. Furieri, A. Bassi, and S. Bonora. Large field of view aberrations correction with deformable lenses and multi conjugate adaptive optics. *Journal of Biophotonics*, 16(12):e202300104, 2023.

[17] Omri Haim, Jeremy Boger-Lombard, and Ori Katz. Image-guided computational holographic wavefront shaping. *Nature Photonics*, 2024.

[18] Karen Hampson, Raphael Turcotte, Donald Miller, Kazuhiro Kurokawa, Jared Males, Na Ji, and Martin Booth. Adaptive optics for high-resolution imaging. *Nature Reviews Methods Primers*, 1:68, 2021.

[19] John W. Hardy. *Adaptive Optics for Astronomical Telescopes*. 1998.

[20] Yi Hua, M. Salman Asif, and Aswin C. Sankaranarayanan. Spatial and axial resolution limits for mask-based lensless cameras. *Opt. Express*, 31(2):2538–2551, 2023.

[21] Seungwon Jeong, Ye-Ryoung Lee, Wonjun Choi, Sungsam Kang, Jin Hee Hong, Jin-Sung Park, Yong-Sik Lim, Hong-Gyu Park, and Wonshik Choi. Focusing of light energy inside a scattering medium by controlling the time-gated multiple light scattering. *Nature Photonics*, 12(5):277–283, 2018.

[22] Na Ji. Adaptive optical fluorescence microscopy. *Nature Methods*, 14:374–380, 2017.

[23] Yonghyeon Jo, Ye-Ryoung Lee, Jin Hee Hong, Dong-Young Kim, Junhwan Kwon, Myunghwan Choi, Moonseok Kim, and Wonshik Choi. Through-skull brain imaging in vivo at visible wavelengths via dimensionality reduction adaptive-optical microscopy. *Science Advances*, 8(30):eabo4366, 2022.

[24] Andrew Jr, Alon Harris, Josh Gross, Ingrida Januleviciene, Aaditya Shah, and Brent Siesky. Optical coherence tomography angiography: An overview of the technology and an assessment of applications for clinical research. *British Journal of Ophthalmology*, 101, 2016.

[25] Sungsam Kang, Pilsung Kang, Seungwon Jeong, Yongwoo Kwon, Taeseok D. Yang, Jin Hee Hong, Moonseok Kim, Kyung-Deok Song, Jin Hyoung Park, Jun Ho Lee, Myoung Joon Kim, Ki Hean Kim, and Wonshik Choi. High-resolution adaptive optical imaging within thick scattering media using closed-loop accumulation of single scattering. *Nature Communications*, 8(1):2157, 2017.

[26] Sungsam Kang, Yongwoo Kwon, Hojun Lee, Seho Kim, Jin Hee Hong, Seokchan Yoon, and Wonshik Choi. Tracing multiple scattering trajectories for deep optical imaging in scattering media. *Nature communications*, 14(1), 2023.

[27] Marie Laslandes, Matthias Salas, Christoph K. Hitzenberger, and Michael Pircher. Increasing the field of view of adaptive optics scanning laser ophthalmoscopy. *Biomed. Opt. Express*, 8(11):4811–4826, 2017.

[28] V. Lauer. New approach to optical diffraction tomography yielding a vector equation of diffraction tomography and a novel tomographic microscope. *Journal of Microscopy*, 205(2):165–176, 2002.

[29] F. C. Lin and M. A. Fiddy. The born–rytov controversy: I. comparing analytical and approximate expressions for the one-dimensional deterministic case. *J. Opt. Soc. Am. A*, 9(7):1102–1110, 1992.

[30] Jerome Mertz. *Introduction to optical microscopy*. Cambridge University Press, 2019.

[31] Sagi Monin, Aswin Sankaranarayanan, and Anat Levin. Exponentially-wide etendue displays using a tilting cascade. *IEEE ICCP*, pages 1–12, 2022.

[32] Ulysse Najar, Victor Barolle, Paul Balondrade, Mathias Fink, Claude Boccara, and Alexandre Aubry. Harnessing forward multiple scattering for optical imaging deep inside an opaque medium. *Nature Communications*, 15(1), 2024.

[33] Tan Nguyen, Mikhail Kandel, Marcello Rubessa, Matthew Wheeler, and Gabriel Popescu. Gradient light interference microscopy for 3d imaging of unlabeled specimens. *Nature Communications*, 8, 2017.

[34] Galya Stern and Ori Katz. Noninvasive focusing through scattering layers using speckle correlations. *Optics Letters*, 44(1):143, 2018.

[35] Jörgen Thaung, Per Knutsson, Zoran Popovic, and Mette Owner-Petersen. Dual-conjugate adaptive optics for wide-field high-resolution retinal imaging. *Opt. Express*, 17(6): 4454–4467, 2009.

[36] Tsai wei Wu and Meng Cui. Numerical study of multi-conjugate large area wavefront correction for deep tissue microscopy. *Opt. Express*, 23(6):7463–7470, 2015.

[37] Gil Weinberg, Elad Sunray, and Ori Katz. Noninvasive megapixel fluorescence microscopy through scattering layers by a virtual incoherent reflection matrix. *Science Advances*, 10(47):eadl5218, 2024.

[38] Emil Wolf. Three-dimensional structure determination of semi-transparent objects from holographic data. *Optics Communications*, 1(4):153–156, 1969.

[39] Tomer Yeminy and Ori Katz. Guidestar-free image-guided wavefront shaping. *Science Advances*, 7(21):eabf5364, 2021.

[40] Lei Zhu, Fernando Soldevila, Claudio Moretti, Alexandra d'Arco, Antoine Boniface, Xiaopeng Shao, Hilton B. de Aguiar, and Sylvain Gigan. Large field-of-view non-invasive imaging through scattering layers using fluctuating random illumination. *Nature Communications*, 13:1447, 2022.